# Cold water anomalies in the middle layer of the northern Taiwan Strait in spring—a numerical approach

Zhonghua Zhao[1] · Jianwei Lin[2] · Jun Fu[3] · Yuwu Jiang[1]

## Abstract

Cold water anomalies were found in the middle layer in the northern Taiwan Strait in the spring of 2015. The cold water was located at a depth of approximately 10–20 m, with warm water situated both above and below this cold water layer. This study investigated this phenomenon using a three-dimensional operational ocean model, in which the sea-surface net heat flux was justified by nudging the appropriate sea-surface temperature (SST) obtained from remote sensing data while maintaining a reasonable modeling skill level with respect to other parameters. The cold water anomaly phenomena were reproduced reasonably well in the model, and the mechanism can be determined by dynamic process analysis and thermal diagnosis of the model results. In the spring of 2015, when the northeasterly monsoon in the Taiwan Strait relaxed and changed to southwesterly, the offshore movement, which was related to both the geostrophic adjustment and Ekman transport in the upper layer, was supplemented by the bottom Ekman onshore transport at the lower level, which resulted in the presence of warm water at the bottom. Meanwhile, the increased solar radiation heated the water at the surface. In the model diagnostic analysis, such warming effects can be demonstrated by cross-strait horizontal advection and vertical diffusion, while in the middle layer, the warming effect was not particularly significant, which was the cause of the cold water anomaly.

**Keywords** Cold water anomaly · Taiwan Strait · Numerical model · SST nudging · Skill assessment · Diagnosis

## Abbreviations

| | |
|---|---|
| SST | Sea-surface temperature |
| TWS | Taiwan Strait |
| SCS | South China Sea |
| ECS | East China Sea |
| TWB | Taiwan Bank |
| PHC | Penghu Channel |
| PHI | Penghu Island |
| CCC | China Coastal Current |
| KBC | Kuroshio Branch Current |
| SCSWC | South China Sea Warm Current |
| ZYR | Zhang-Yun Rise |
| PTI | Pingtan Island |
| TFOR | TWS Nowcast/Forecast System |
| MB | Mean bias |
| CC | Correlation coefficient |
| RMSD | Root-mean-squared difference |
| WS | Willmott skill |
| WOA | World Ocean Atlas climatological SST data |
| MUR | Multiscale Ultrahigh Resolution daily SST data |
| NCEP | National Centers for Environmental Prediction SST data |

✉ Yuwu Jiang
ywjiang@xmu.edu.cn

1 State Key Laboratory of Marine Environmental Science, College of Ocean and Earth Sciences, Xiamen University, Xiamen 361102, People's Republic of China

2 Fisheries Research Institute of Fujian, Xiamen 361013, People's Republic of China

3 Hangzhou Xi'ao Environmental Sci-tech Co., Hangzhou 310012, People's Republic of China

## 1 Introduction

The Taiwan Strait (TWS) is a water channel linking the South China Sea (SCS) with the East China Sea (ECS). The TWS's bottom bathymetric topography is spatially variable with an average depth of approximately 60 m (Fig. 1). The Taiwan Bank (TWB) located in the southern part of the TWS is around 20-m deep. The Penghu Channel (PHC) is between Penghu Island
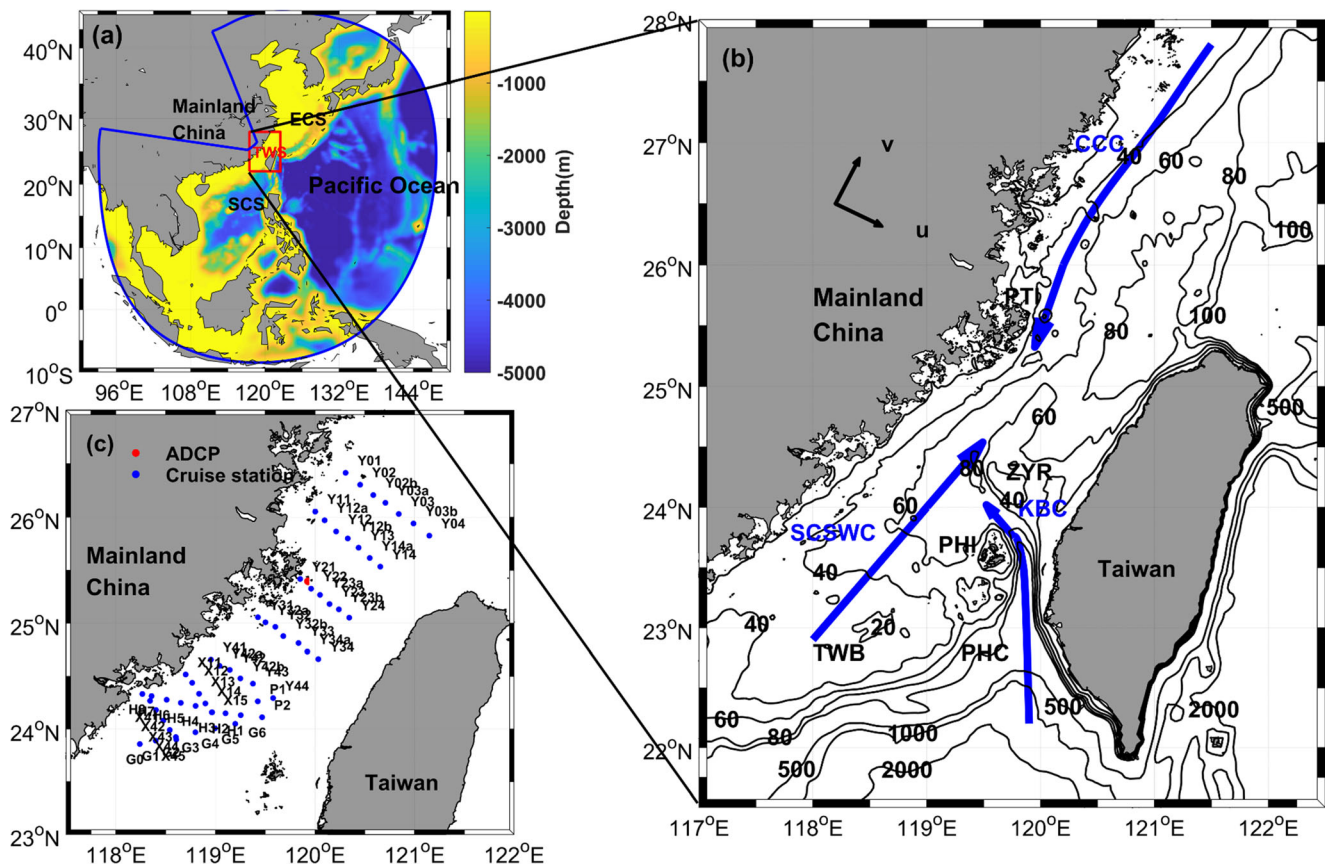
Fig. 1 TFOR's modeling domain (a), bottom topography (units: m) of the TWS (b), and observation stations in the TWS (c). (a) The blue line shows the TFOR domain, and the red box shows the location of the zoomed-in view (b). ECS, SCS, and TWS denote the East China Sea, South China Sea, and Taiwan Strait, respectively. (b) TWB, PHC, PHI, ZYR, and PTI denote the Taiwan Bank, Penghu Channel, Penghu Island, Zhangyun Ridge, and Pingtan Island. Major currents in the TWS

including the China Coastal Current (CCC), the Kuroshio Branch Current (KBC), and the extension of the South China Sea Warm Current (SCSWC) are denoted by solid blue arrows. The arrows of *u* and *v* delineate the direction of the analyzed velocity that crosses and moves along the TWS. (c) Blue dots are cruise stations, and the red dot represents the bottom-mounted ADCP

(PHI) and Taiwan in the southeastern TWS. The TWS is in the subtropical monsoon regime with northeasterly wind dominating in the winter and southwesterly wind prevailing in the summer. The monsoon, circulation pattern in the northern SCS, riverine water input, and Kuroshio intrusion are all related to the temporal and spatial variation in the circulation pattern of the TWS along with its complex bottom topography (Hong et al. 2011). Generally, there are three primary currents in the TWS, including the China Coastal Current (CCC) in the western TWS, the Kuroshio Branch Current (KBC), and the extension of the South China Sea Warm Current (SCSWC). Hu et al. (2010) reviewed more than 150 studies and summarized the current pattern and water mass transport in the TWS. In their work, they found that the general current pattern can be influenced by wind conditions associated with different synoptic processes. Wu et al. (2007) reproduced synoptic, seasonal, and interannual TWS current variations with a numerical model that has a horizontal grid size that varies from 3 to 10 km with finer resolution near the center of the TWS and found that the Zhang-Yun Rise (ZYR) blocks a portion of the southward CCC. In general, the CCC

flows southwestward along the western coast of the TWS. Occasionally, there is an offshore branch located off Pingtan Island (PTI) in the western strait and extending to the ZYR, which then returns northeastward, forming a U-shaped flow pattern in the northern TWS. With the use of an operational numerical model, the separation of the CCC was reproduced by Wang et al. (2016) and Lin et al. (2016). The separation mechanisms were described by Liao et al. (2013) as a geostrophic adjustment, and Oey et al. (2014) characterized them as a stationary Rossby wave. Jan et al. (2006, 2002) reported that the KBC is usually restricted to the PHC when the northeasterly wind prevails in winter. The weakening of the northeasterly wind in February and March releases the blocked KBC, which can then move northward, while the CCC remains confined to the west coast of the TWS. Hu et al. (2003) identified four upwelling regions in the TWS in the summer months, with one along the southwestern coast of the TWS, one along the northwestern coast of the TWS, another near the TWB, and a fourth one around the Penghu Islands. They are induced primarily by the Ekman transport mechanism during the summer monsoon season.

Several numerical models of the TWS have been developed to evaluate or predict physical processes and characteristics in the strait. Jan et al. (2002) presented a numerical model to reproduce salient features of seasonal variations in the circulation of the TWS based on observational data. Jiang et al. (2011) used a nested circulation model based on the Princeton Ocean Model (POM) to study the upwelling events in the southern TWS and revealed that the colder water carried to the near-surface layer can be diffused up into the surface layer as a result of tidal mixing, which forms the TWB upwelling. Based on the POM for the TWS, Hu et al. (2011) explained the variable structures of temperature, salinity, and water mass in the southwestern TWS during the summer. Oey et al. (2013) developed a data-assimilated Taiwan Ocean Prediction (ATOP) model that simulated sea-surface height, three-dimensional currents, temperature, salinity, and turbulent mixing. Lin et al. (2016) assessed the overall performance of the TWS Nowcast/Forecast System (TFOR) and found that the model can be used to obtain three-dimensional results in terms of temperature, salinity, and velocity with a reasonable degree of accuracy. In addition to these physical studies, mechanisms related to the physical-biological processes in the TWS have also been studied based on the TFOR, such as the TWS cold disaster in 2008 by Liao et al. (2013), the cape and canyon effect on the upwelling off the northwestern coast of the TWS proposed by Chen et al. (2014), the coupled physical-biological model used by Wang et al. (2016, 2013) to simulate nutrient fate in summer and winter blooms in the TWS, and a mechanism proposed by Lu et al. (2015) for the winter Luzon bloom in the oligotrophic SCS.

Temperature inversion occurs when the vertical temperature profile shows colder water in the upper layer and warmer water in the lower layer. It is usually accompanied by a salinity profile where fresh water is present in the upper layer, and saline water comprises the lower layer while stable stratification is maintained (Chen et al. 2006). The phenomenon has also occurred in the TWS during autumn, winter, and spring (Qiu et al. 2012; Xiao et al. 2002; Yan 1991) with different spatial and temporal variations (Hao et al. 2010). There are generally two formation mechanisms responsible for temperature inversion, including the generation of cold and fresh water in the surface layer from a significant cooling effect and local precipitation in winter (Hao et al. 2010; Ueno and Yasuda 2005) and the advection of cold and fresh water over warm and saline water by ocean currents (Thadathil and Gosh 1992). Guan (1999) and Qiu et al. (2012) noted that the temperature inversion in the TWS is primarily generated by the second mechanism.

The cold water anomaly in the middle layer, which is associated with temperature inversion, refers to relatively cold water located in the middle layer with warm water

found in the upper and lower (bottom) layers. Previous studies have focused on this phenomenon that was in the East China Sea and the Yellow Sea. They proposed that increasing temperatures in both the surface and bottom layers in spring and the advection of cold water in the middle layer are the primary reasons for the phenomenon (Ding and Lan 1995; Wang et al. 2002; Xu et al. 2000). However, causal links were provided in a relatively descriptive and general manner. The intrinsic mechanisms attributable to specific conditions that could create the cold water anomaly in the middle layer in the TWS have not been reported prior to this study.

In this study, a numerical model based on TFOR was used to reproduce and analyze the middle-layer cold water anomaly found in the northern TWS in the spring of 2015. The remainder of this paper is organized in the following manner. The observational data and model system are outlined in Section 2. The model performance is evaluated in Section 3. The mechanism analysis of the cold water anomaly in the middle layer is presented in Section 4, and the conclusions are summarized in Section 5.

## 2 Data and model

### 2.1 Statistical methods

Several statistical metrics are introduced to evaluate model performance with the use of observational data. The mean bias (MB) gives the mean difference between the modeling results and observed data. The correlation coefficient (CC) shows the collinearity relationship between their time series, whereas the root-mean-squared difference (RMSD) provides the absolute difference between the two datasets, and the Willmott skill (WS, Willmott 1981) quantifies the extent of agreement between them, the value of which varies from 0 to 1, which represents a corresponding range from no agreement to perfect agreement, respectively. The definition of these statistical metrics is as follows:

$$MB = \langle m - o \rangle \tag{1}$$

$$CC = \left[ \sum_{i=1}^{n} (m_i - \langle m \rangle)(o_i - \langle o \rangle) \right] / (n \sigma_m \sigma_o) \tag{2}$$

$$RMSD = \sqrt{\left[ \sum_{i=1}^{n} (m_i - o_i)^2 \right] / n} \tag{3}$$

$$WS = 1 - \left\langle (m - o)^2 \right\rangle / \left\langle \left( |m - \langle o \rangle| + |o - \langle o \rangle| \right)^2 \right\rangle \tag{4}$$

where $m$ and $o$ represent the time series of the model results and observational cruise data, respectively. In this study, $n$ is the number of samples, and $\sigma$ represents the standard deviation. Angled brackets denote a mean operator.

## 2.2 Observations

An investigation cruise was organized by Xiamen University and served by R/V Yanping No. 2 from March 30 to April 3, 2015. There were 60 hydro-cast stations within 9 sections. The time series of the vertical current velocity profile at 1-h intervals from February 19 to March 31, 2015, was obtained from a bottom-mounted acoustic current profiler (ADCP) deployed off the coast of PTI (Fig. 1c).

## 2.3 Model system

Based on the Regional Ocean Modeling System (Shchepetkin and McWilliams 2003; Shchepetkin and McWilliams 2005), a free-surface, terrain-following, primitive equation ocean circulation model under hydrostatic and Boussinesq assumptions, the TFOR of the TWS was developed and maintained (Chen et al. 2014; Lin et al. 2016; Lu et al. 2015; Wang et al. 2016; Wang et al. 2013). The modeling domain covers the northwestern Pacific Ocean using curvilinear-orthogonal grids with a 45-km resolution at the open boundary and a 1.5-km resolution in the TWS (Fig. 1a). A total of 30 vertical layers were derived using a stretching function, where $\theta_s = 3.0$, $\theta_b = 0.4$, and $h_c = 10m$ following the S-coordinate scheme (Song and Haidvogel 1994). Chapman (1985) boundary conditions were used for free surfaces, Flather boundary conditions (Flather 1976) were used for two-dimensional momentum, and clamped boundary conditions were employed for three-dimensional momentum and tracers. The lateral open boundary, including sea level, velocity, temperature, and salinity, was obtained from MyOcean (http://ecmwf.int/en/research/projects/myocean) in addition to the initial fields on January 1, 2014. Tidal forcing with 10 main tidal components ($M_2$, $S_2$, $N_2$, $K_2$, $K_1$, $O_1$, $P_1$, $Q_1$, $M_f$, and $M_m$) was provided by TPXO7.0 (Egbert and Erofeeva 2002) at the lateral boundary. The monthly mean discharges of the major rivers along the mainland coast, including the Yangtze, Pearl, Yalu, Liaohe, Luanhe, Ou, Minjiang, Jiulong, and Hanjiang Rivers, were also included in the model, with their salinities set at zero.

The model bathymetry was obtained by combining 25 digitized ocean charts from the Maritime Safety Administration (China), the 0.5′ gridded bathymetry of the TWS (http://www.odb.ntu.edu.tw), and the ETOPO2v2 data published by the National Geophysical Data Center at the National Oceanic and Atmospheric Administration (NOAA, https://www.ngdc.noaa.gov). A weak filter (rfact = 0.35) was applied to smooth the bathymetry to reduce the unexpected diapycnal mixing error.

The air-sea flux, including momentum flux, heat flux, and freshwater flux, was interpolated from data provided by the Weather Research and Forecast Model (WRF) with 0.2° resolution in Fujian Marine Forecasts (http://www.fjmf.gov.cn/Ocean863Web_MAIN/default.aspx#szyb). The details of the model settings can be found in Lin et al. (2016). Moreover, in

this study, the sea-surface net heat flux ($Q_{NET}$) was justified by nudging the referenced sea-surface temperature (SST) $\left(T_s^{ref}\right)$ with a relaxation coefficient to improve the modeling performance of temperature.

$$Q_{NET} = Q'_{NET} + dQdSST \cdot \left(T_S^{ref} - T_S\right) \qquad (5)$$

where $Q'_{NET}$ is the net heat flux that can be calculated from the bulk flux algorithm (Fairall et al. 1996) and $dQdSST$ is the net heat flux sensitivity to the SST (Barnier et al. 1995). $T_S$ is the SST from the model, and $T_S^{ref}$ is the referenced SST, which is the nudging target. Three candidates were evaluated to determine the appropriate $T_S^{ref}$, including the World Ocean Atlas climatological SST data (WOA, https://data.nodc.noaa.gov/woa/), the Multiscale Ultrahigh Resolution daily SST data (MUR, https://data.nodc.noaa.gov/ghrsst/L4/GLOB/JPL/MUR/), and the National Centers for Environmental Prediction SST data (NCEP, https://data.nodc.noaa.gov/ncep/), all of which are from the National Oceanographic Data Center of NOAA. Figure 2 presents a comparison of the observed SST from the investigation cruise and the referenced SST, whereas the corresponding statistical comparison metrics (values of MB, CC, RMSD, and WS) are presented in Table 1. The SST based on the MUR data was found to be the best match with the observational SST data (Fig. 2) with higher CC and WS values of 0.72 and 0.84, respectively, and lower MB and RMSD values of 0.31 °C and 1.70 °C, respectively, whereas the WOA and NCEP datasets did not display such performance. Consequently, the MUR SST data were used for the nudging process to justify the model sea-surface net heat flux, $Q_{NET}$. The value of $dQdSST$ was set to 150 ($Wm^{-2\,\circ}C^{-1}$) in the research domain, which means the relaxing time was approximately 19 days in the TWS (Barnier et al. 1995). With the net heat flux adjusted by the MUR SST data, the model was hot-started from the TFOR restart file on January 1, 2014.

# 3 Model evaluation

## 3.1 Velocity comparison

Figure 3 compares velocities from the modeling results and the buoy (location is presented in Fig. 1c) from February 25 to April 5, 2015. The velocities at the surface, middle, and bottom layers and the vertically averaged velocity were rotated to the cross-strait (u) and along-strait (v) directions (Fig. 1b). Modeled velocities with and without nudging the SST and tidal influence (36-h low-pass-filtered) were all involved in the comparisons. The temporal variation of the wind at the buoy is also presented.

As shown by the observed data, both the cross-strait (**u**) and along-strait (**v**) velocity components (especially the along-
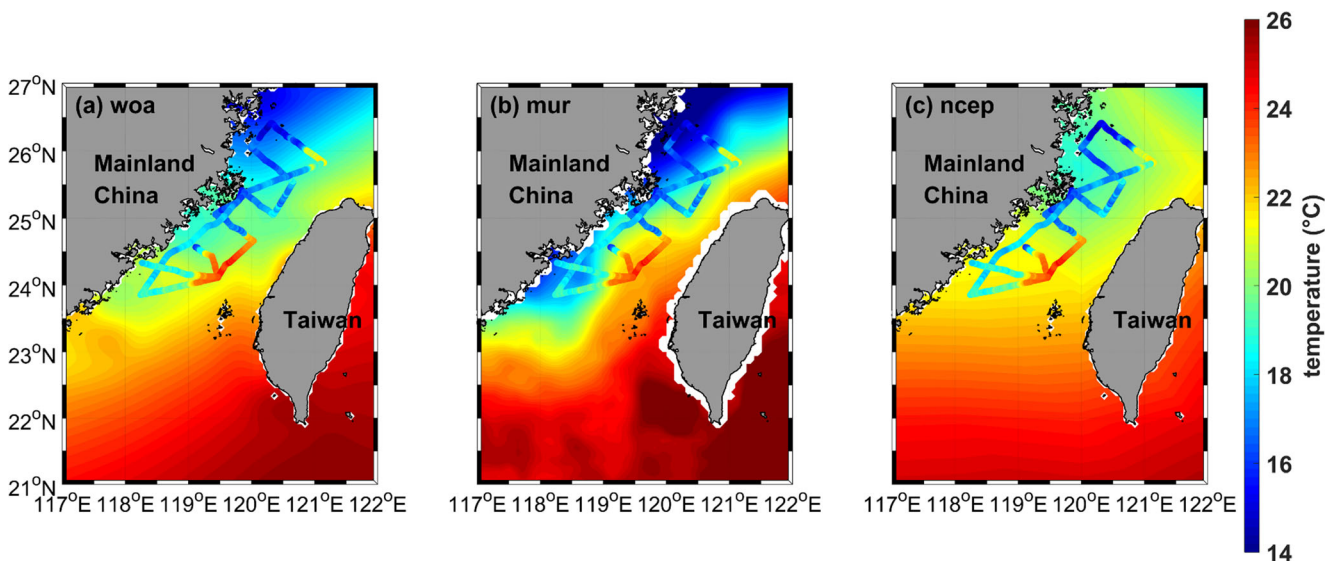
**Fig. 2** Comparison of referenced sea-surface temperature $T_S^{ref}$ from three different datasets ((**a**) WOA, (**b**) MUR, and (**c**) NCEP, base map) and the measured SST along the cruise path from March 30 to April 3, 2015

strait component) were significantly related to the temporal variation of the wind. Vertical uniformity in the along-strait velocity component (**v**) for both the observations and model results was also determined (Fig. 3b–3d). The along-strait component (**v**) turned from negative/southward to positive/northward over the entire water column during the relaxation of the northeasterly monsoon (i.e., from March 10 to March 17), which indicated the along-strait current in the TWS was dominated by both wind stress and a northward pressure gradient. Meanwhile, when the northeasterly wind switched to southwesterly, the cross-strait velocity component (**u**) at the surface tended to be opposite of that at the bottom (e.g., March 18–19 and March 31 to 1 April). This offshore velocity component (positive u) at the surface indicated that there was an offshore branch of the coastal current at the western strait. This phenomenon of current separation was reported and evaluated in several studies (e.g., Lin et al. 2016; Wang et al. 2016; Wu et al. 2007).

The model results of velocity at the buoy site showed the same temporal tendency as the observations (Fig. 3b–3q). Table 2 provides the corresponding statistical comparison metrics. Without nudging the SST, the MB, CC, RMSD, and WS, results for the vertically mean along-strait velocity component (**v**) between the observational data and model

outputs were −0.075, 0.861, 0.245, and 0.919, respectively, and those for the vertically mean cross-strait velocity component (**u**) were −0.048, 0.497, 0.122, and 0.678, respectively. With tidal influence removed, the MB, CC, RMSD, and WS values were −0.073, 0.877, 0.167, and 0.922 for the vertically mean along-strait velocity component (**v**) and −0.048, 0.132, 0.067, and 0.390 for the vertically mean cross-strait velocity component (**u**), respectively. The modeling results showed that the along-strait velocity component (**v**) was reproduced better than the cross-strait component (**u**). In a word, the statistical metrics for model outputs from nudging the SST were quite comparable with those without nudging the SST.

In general, the model captured the basic current pattern in the TWS, and the volume flux of CCC in the model was reasonable (Lin et al. 2016). The observation and model results both indicated that the along-strait velocity component (**v**) was stronger than the cross-strait component (**u**), and it had a correspondingly larger CC value. The comparisons also revealed that the observations had more positive values for both the velocity components than the model results, especially in the surface layer, which indicated that the northward and offshore current in the model were weaker than that in the observations. This may be due to the stronger and more uniform northeasterly wind in the model than the observations (Fig. 3a).

### 3.2 Tracers comparison

The in situ measurements described in Section 2.2 indicated some important characteristics in the springtime TWS seawater properties (Fig. 4). The cold and fresh CCC flowed in the western portion of the sections, whereas the warm and salt southern water transported by both the KBC and SCSWC occupied the middle and eastern parts of the sections. Fresh

**Table 1** Comparison metrics between the observed SST and the referenced SST from three different datasets (WOA, MUR, and NCEP)

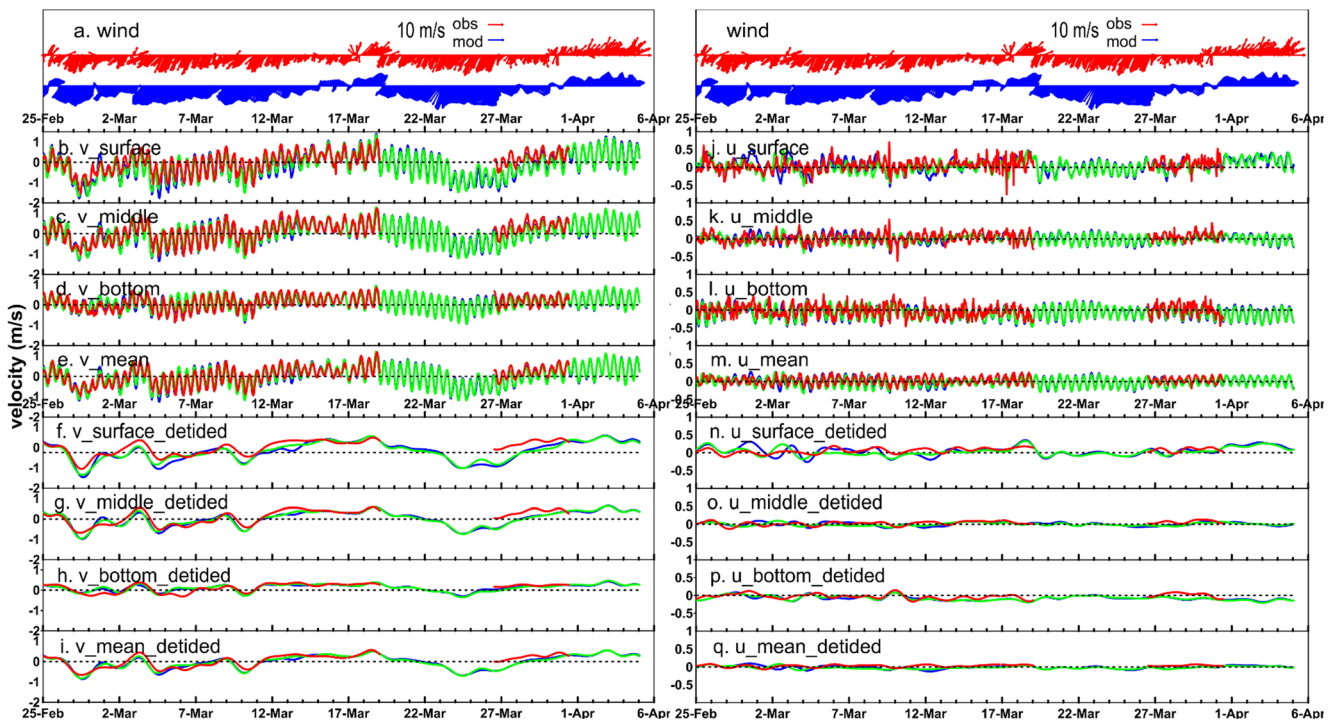| Dataset | MB(°C) | CC | RMSD(°C) | WS |
|---------|--------|------|----------|------|
| WOA | 1.00 | 0.61 | 2.20 | 0.66 |
| MUR | 0.31 | 0.72 | 1.70 | 0.84 |
| NCEP | 2.00 | 0.62 | 2.80 | 0.56 |

**Fig. 3** Wind variation at the buoy from February 25 to April 5, 2015 (**a**). The red vectors indicate the observed wind, and the blue vectors indicate the WRF wind. Current verification with and without tidal influence in the along-strait v (**b**–**i**) and cross-strait u (**j**–**q**) directions for surface, middle, and bottom layers, in addition to the mean depth. The red lines indicate the observed velocity; the blue lines and green lines indicate the modeled velocity with and without nudging the SST, respectively. The u and v direction and location of the buoy are shown in Fig. 1

and cold water of the CCC stretched nearly to the northern part of the TWS eastern coast (e.g., sections Y1 and Y2), whereas it was limited to within 60 km off the western coast in the middle part of the strait (e.g., sections Y3, Y4, X1). Front was formed at about 40–100 km offshore, where the two water masses converged with dense tracer contours (salinity and temperature) stretching from the eastern part of the sections at the surface to the western part of the sections at the bottom (Fig. 4). Temperature and salinity were vertically homogenous at multiple offshore stations, including stations G5, H2,

**Table 2** Comparison metrics between the observed and modeled velocity components in the surface, middle, and bottom layers, as well as the vertically mean velocity components at the station of the bottom-mounted ADCP (Fig. 1c). Modeled velocity with and without nudging SST (NUG and NoNUG) as well as removing tidal influence (36-h low-pass-filtered) were all involved. The u and v directions are shown in Fig. 1b

| | Metrics | MB (m/s) | | CC | | RMSD (m/s) | | WS | |
|---|---|---|---|---|---|---|---|---|---|
| Direction | Layer | NoNUG | NUG | NoNUG | NUG | NoNUG | NUG | NoNUG | NUG |
| U | Surface | −0.039 | −0.016 | 0.373 | 0.348 | 0.187 | 0.200 | 0.617 | 0.603 |
| | Middle | −0.034 | −0.022 | 0.421 | 0.427 | 0.138 | 0.137 | 0.640 | 0.652 |
| | Bottom | −0.049 | −0.054 | 0.429 | 0.416 | 0.188 | 0.195 | 0.654 | 0.645 |
| | Mean | −0.048 | −0.038 | 0.497 | 0.487 | 0.122 | 0.120 | 0.678 | 0.683 |
| U (no tide) | Surface | −0.037 | −0.014 | 0.374 | 0.373 | 0.108 | 0.120 | 0.594 | 0.572 |
| | Middle | −0.034 | −0.021 | 0.284 | 0.358 | 0.071 | 0.067 | 0.513 | 0.605 |
| | Bottom | −0.051 | −0.055 | 0.627 | 0.553 | 0.077 | 0.084 | 0.707 | 0.663 |
| | Mean | −0.048 | −0.037 | 0.132 | 0.173 | 0.067 | 0.064 | 0.390 | 0.407 |
| V | Surface | −0.215 | −0.219 | 0.834 | 0.836 | 0.385 | 0.401 | 0.871 | 0.867 |
| | Middle | −0.106 | −0.105 | 0.857 | 0.858 | 0.286 | 0.288 | 0.913 | 0.914 |
| | Bottom | 0.002 | −0.001 | 0.766 | 0.776 | 0.226 | 0.222 | 0.872 | 0.879 |
| | Mean | −0.075 | −0.077 | 0.861 | 0.863 | 0.245 | 0.249 | 0.919 | 0.919 |
| V (no tide) | Surface | −0.213 | −0.217 | 0.862 | 0.845 | 0.302 | 0.326 | 0.857 | 0.844 |
| | Middle | −0.103 | −0.101 | 0.876 | 0.873 | 0.201 | 0.203 | 0.914 | 0.912 |
| | Bottom | 0.005 | 0.002 | 0.774 | 0.838 | 0.129 | 0.114 | 0.859 | 0.887 |
| | Mean | −0.073 | −0.074 | 0.877 | 0.874 | 0.167 | 0.171 | 0.922 | 0.919 |
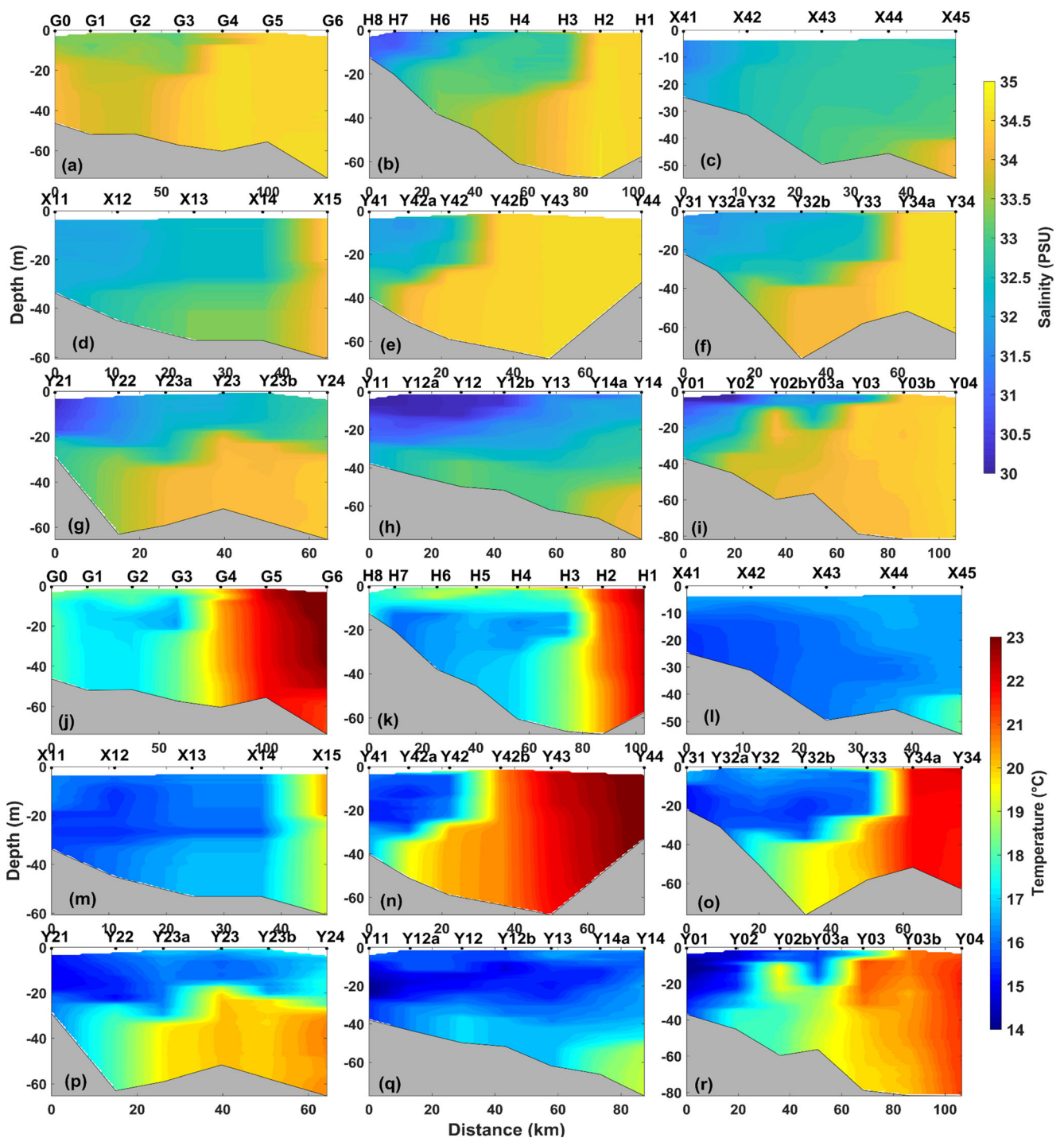
**Fig. 4** Observed salinity (**a**–**i**) and temperature (**j**–**r**) distributions along each section of the cruise from March 30 through April 3, 2015. The cruise sections are presented in Fig. 1c

Y43, and Y34a. Temperature inversion appeared in the northern sections with cold water at the surface and warm water at the bottom (Fig. 4n–4r). However, the static stability could be maintained with normal salinity patterns (Fig. 4e–4i). The cold water anomalies in the middle layer (~20 m) were evident in sections Y1 and Y2 (Fig. 4q and p), which were about 10-m thick and extended to around 60–80 km offshore.

Figure 5 shows modeled salinity distributions along each section without nudging the SST, which were virtually the same as the modeled salinity distributions with nudging of the SST. Figures 4 and 5 indicate that model results captured the salinity distribution patterns in the TWS with respect to the observational data. The statistical analyses revealed that without nudging the SST, the MB, CC, RMSD, and WS values for
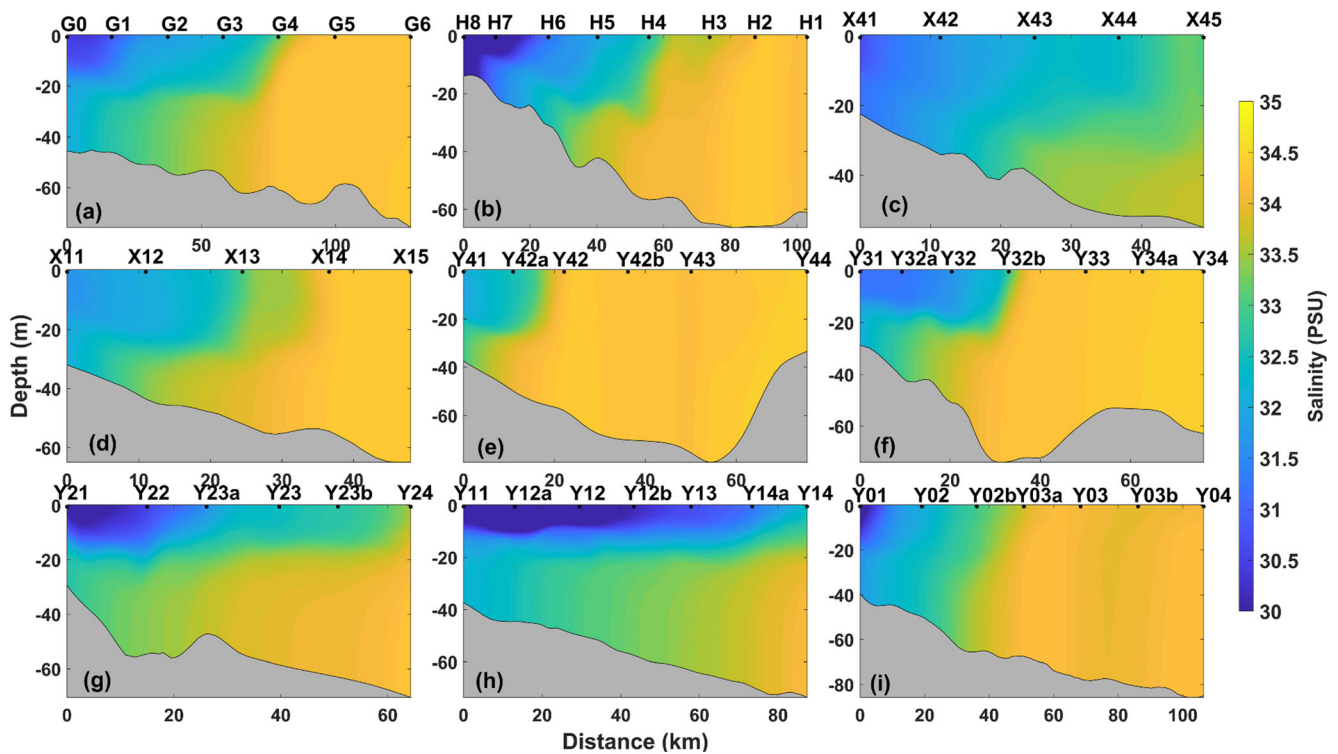
**Fig. 5** Distributions of modeled salinity without nudging the SST along each section on the corresponding cruise date from March 30 through April 3, 2015; the results with nudging the SST were virtually the same. The cruise sections are presented in Fig. 1c

the salinity simulation in the TWS were − 0.01 PSU, 0.83, 0.65 PSU, and 0.91, respectively. With nudging process, those values became −0.20 PSU, 0.83, 0.66 PSU, and 0.90, respectively. This comparability indicated that the SST nudging process could maintain a reasonable modeling skill with respect to salinity.

Figure 6 provides a comparison of temperature distributions for each section from the modeling outputs with and without nudging of the SST. Without nudging, the modeled temperature was overestimated compared with the observations over the entire TWS water column, and the cold water anomalies in the middle layer were not well reproduced (Fig. 6a–6i). In this case, the MB, CC, RMSD, and WS values for the temperature simulation in the TWS were 3.70, 0.88, 3.86, and 0.61 °C, respectively. The relatively high CC indicated that the model without nudging of the SST captured the same spatial structure of the temperature distribution in the TWS as the observations to some degree, whereas the high MB might be related to the inaccuracy of the sea-surface net heat flux estimates in the model. With the nudging process described in Section 2.3, model performance with respect to temperature has been improved (Fig. 6j–6r) with the MB, CC, RMSD, and WS values being 0.71, 0.93, 1.08, and 0.94 °C, respectively. Therefore, nudging of the SST significantly improved the modeling performance with respect to temperature.

In general, with nudging of the SST, the spatial distributions of temperature in the TWS during the observation period

were captured. The cold water anomalies in the middle layer along sections Y1 and Y2 (Fig. 6q and p) were reproduced reasonably well, whereas other parameters, such as salinity and velocity, maintained their original values.

# 4 Analysis of middle-layer cold water anomaly

## 4.1 Dynamic process analysis

To find the mechanism of the cold water anomalies in the middle layer of sections Y1 and Y2, modeled distributions of cross-strait (u) and along-strait (v) velocity components in section Y1 from March 30 to April 2, 2015, with nudging of the SST are plotted in Fig. 7, where the contours identify the factors behind the variation of the temperature distribution along the section. To diminish the artificial effects induced by SST nudging within the modeled physical process, the simulation results with a much weaker SST nudging, i.e., the relaxation time is set to 120 days, beginning at March 1, 2015, are used to do the analysis. Although the modeled temperature with weak nudging presented in Fig. 7 is a little bit higher than that with strong nudging in Fig. 6, phenomenon of the middle-layer cold water anomalies is also reasonably reproduced, and the momentum and tracers diagnoses are almost the same (figures not shown here).
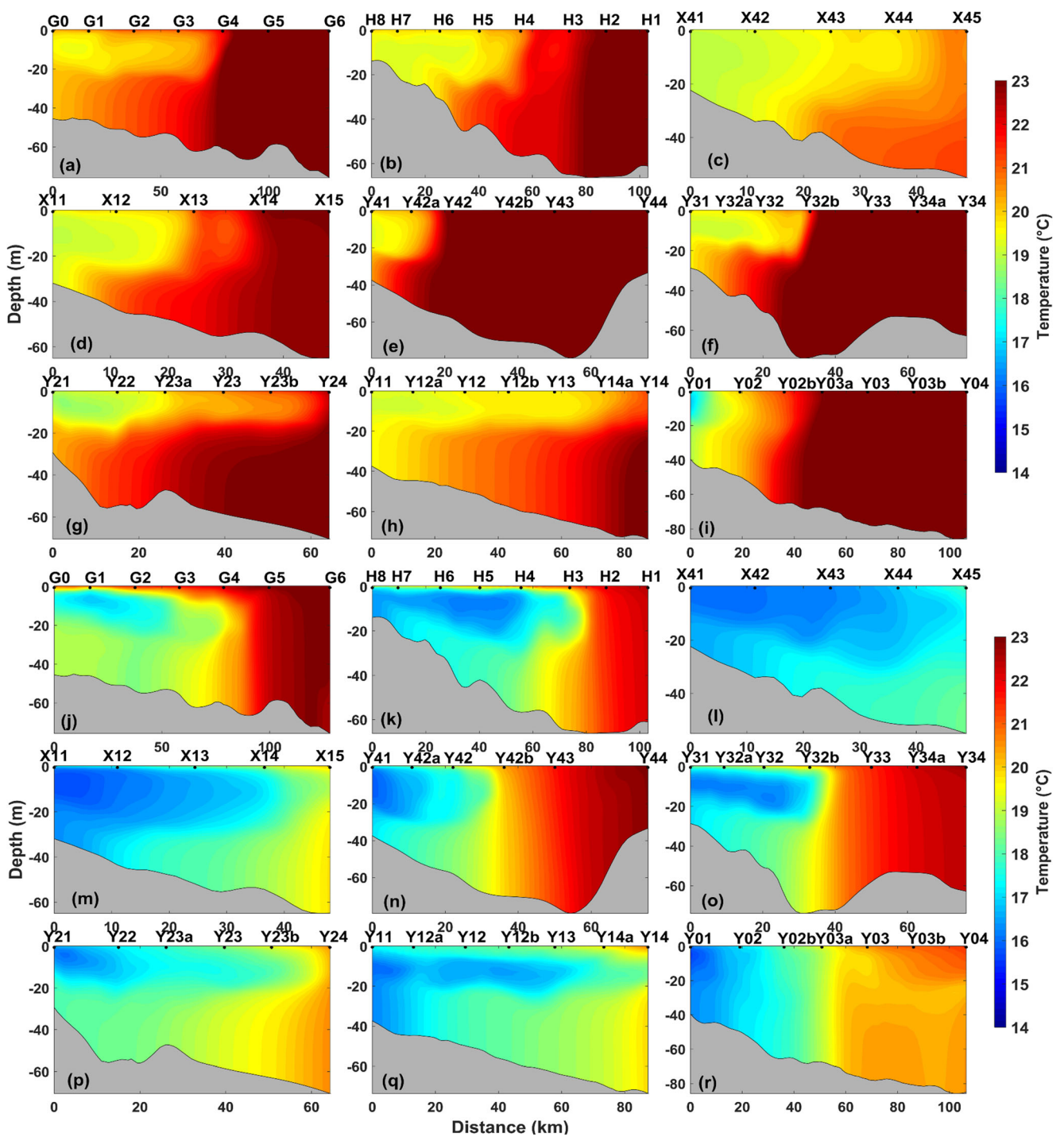
**Fig. 6** Distributions of modeled temperature along each section without (**a–i**) and with (**j–r**) nudging the SST on the corresponding cruise date from March 30 through April 3, 2015. The cruise sections are presented in Fig. 1c

The modeled cross-strait velocity component (**u**) was positive/offshore within the upper 15 m and negative/onshore in the lower layer of the section from March 31 to April 2 (Fig. 7b–7d). It is worth noting that the offshore velocity component (positive u) was an indicator of coastal current separation. The current separation is consistent with the studies by Lin et al. (2016) and Wang et al. (2016). They reported that the CCC flows

southwestward along the western coast of the TWS and has an offshore branch that leaves the main stream and flows to the central strait when the northeasterly wind relaxes or switches to southwesterly. The mechanism for the offshore velocity proposed by Liao et al. (2013) is due to a geostrophic adjustment. In the spring of 2015, the monsoon in the TWS operated northeasterly from March 20 to March 30, and it relaxed roughly on
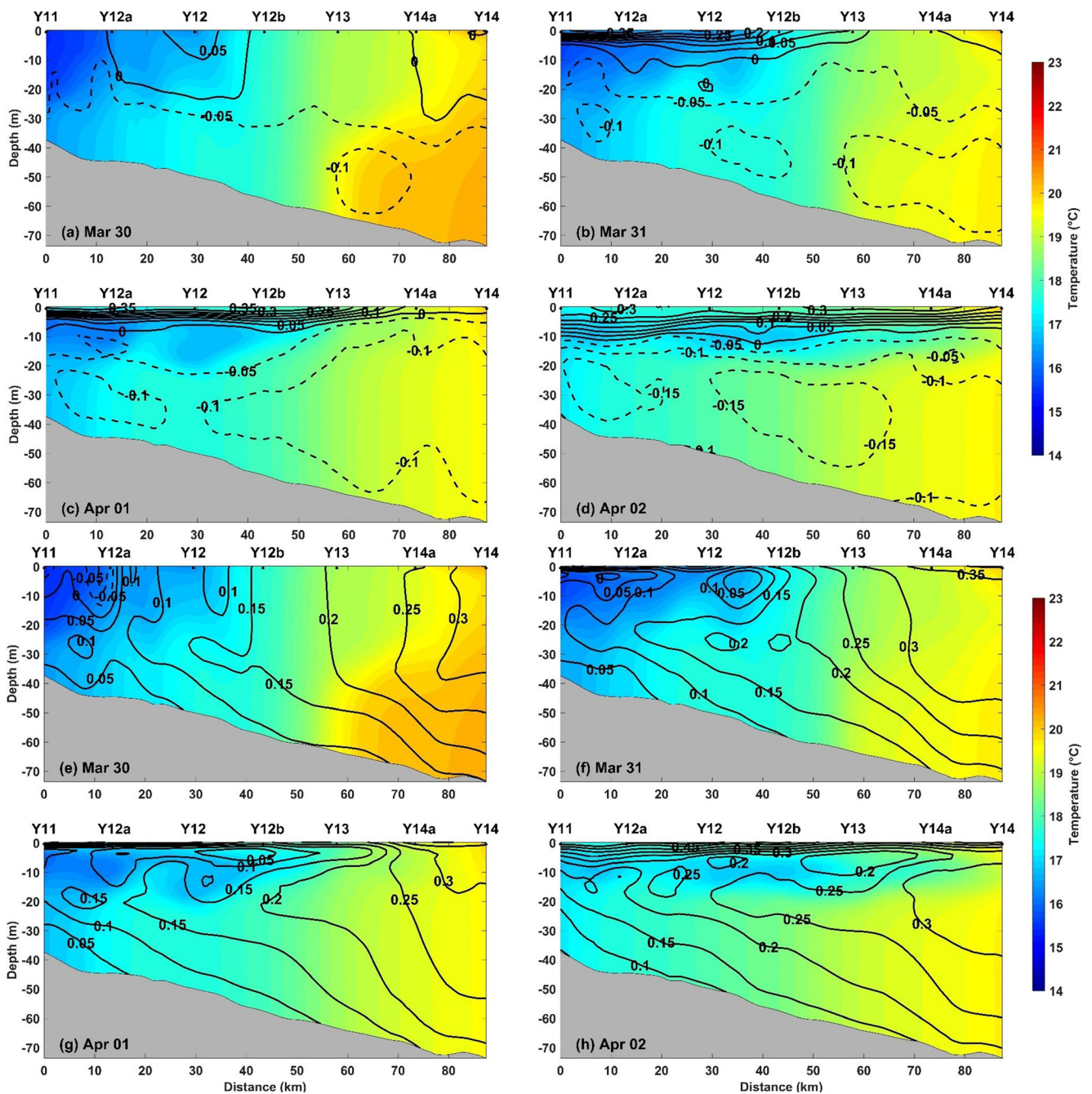
**Fig. 7** Modeled cross-strait (**u**) velocity component along section Y1 ((**a**–**d**) offshore is positive with solid contours; onshore is negative with dashed contours; units: m/s) and along-strait (**v**) component across section Y1 ((**e**–**h**) northward is positive with solid contours; southward is negative with dashed contours; units: m/s) with modeled temperature distributions (shadow) along the section during March 30 to April 2, 2015. The u, v direction and location of section Y1 are shown in Fig. 1. Model results with weak nudging of 120-day relaxation time starting at March 1, 2015, are used for the analysis

March 27 and switched to southwesterly near March 31 (Fig. 3a). On March 30, when the northeasterly wind relaxed, except for the surface current along the coast was flowing south and extending offshore (Fig. 7a and e), the current in the TWS was flowing northward and onshore. From March 31 to April 2, when the wind came from the southwest, the offshore velocity component at the surface could extend to all the sections due to the Ekman

transport. The offshore current on March 30 was related to geostrophic adjustment. Cushman-Roisin and Beckers (2011) proposed that the distance over which the light nearshore water spills offshore in the adjusted state is the radius of deformation (Eq. (6)).

$$R = \sqrt{g'H}/f \qquad (6)$$

In Eq. (6), $g'$ is the reduced-gravity constant $g' = g \nabla \rho / \rho_0$, where $g$ is the gravitational acceleration, $\rho_0$ is the reference density, and $\nabla \rho$ is the characteristic density difference along section Y1. $H$ is the characteristic depth of the light nearshore water, and $f$ is the local Coriolis parameter. The estimate of the radius of deformation gave the offshore moving distance of ~20 km, which coincided with the modeled offshore velocity component (positive $u$, Fig. 7a). In addition, supplementary bottom Ekman onshore transport was also induced (Fig. 3p and Fig. 7a–d), whereas the along-strait velocity component ($v$) was positive/northward in all the sections (Fig. 3f–i and Fig. 7e-h). This presence of the uniformly northward along-strait velocity component (positive $v$) in the TWS during the relaxation of the northeasterly wind was consistent with studies by Jan et al. (2006); Jan et al. (2002); Oey et al. (2014); Wang et al. (2016); and Wu et al. (2007). In addition, Yang (2007) proposed that there is a northward pressure gradient force in the TWS all the year around.

The vertical distributions of temperature along the section Y1 from March 30 to April 2 are also provided in Fig. 7 (shadow map). The basic features included the presence of warmer water in the eastern part of the section, whereas colder water was found in the western part. The offshore current related with the geostrophic adjustment carried the cold water

to 30 km in the upper 25 m on March 30 when the northeasterly wind relaxed, and the surface Ekman effect transported it further offshore to 80 km within the upper 15 m under the southwesterly wind. In the bottom layer, the onshore velocity component (negative $u$) transported warm water onshore. As a result, the front tilted, stretching offshore within the upper 15 m and onshore in the lower layer of the section. Meanwhile, the uniformly northward along-strait velocity component (positive $v$) over the entire section carried more southern warm water significantly during this period and resulted in a gradual increasing of temperature throughout the section. It is also important to note that the temperature in the thin surface layer (approximately 0–10-m depth) increased from April 1 to April 2 (Fig. 7c and d), although the cold water was moving offshore from the western part of the section in the upper layer. This process is described in greater detail in the following section.

To further demonstrate the roles and occurrence sequence of geostrophic adjustment as well as the surface and bottom Ekman effects during the development of the phenomenon, modeled time series of cross-strait ($u$, Eq. (7)) and along-strait ($v$, Eq. (8)) momentum budget terms in the surface and bottom layers at station Y12a are presented in Fig. 8.

$$\overbrace{\frac{\partial u}{\partial t}}^{U_{accel}} = \overbrace{-\left(u\frac{\partial u}{\partial x} + v\frac{\partial u}{\partial y} + w\frac{\partial u}{\partial z}\right)}^{U_{adv}} + \overbrace{fv}^{U_{cor}} \overbrace{-\frac{1}{\rho_0}\frac{\partial p}{\partial x}}^{U_{prsgrd}} + \overbrace{\frac{\partial}{\partial x}\left(A_h\frac{\partial u}{\partial x}\right) + \frac{\partial}{\partial y}\left(A_h\frac{\partial u}{\partial y}\right)}^{U_{hvisc}} + \overbrace{\frac{\partial}{\partial z}\left(A_z\frac{\partial u}{\partial z}\right)}^{U_{vvisc}} \tag{7}$$

$$\overbrace{\frac{\partial v}{\partial t}}^{V_{accel}} = \overbrace{-\left(u\frac{\partial v}{\partial x} + v\frac{\partial v}{\partial y} + w\frac{\partial v}{\partial z}\right)}^{V_{adv}} \overbrace{-fu}^{V_{cor}} \overbrace{-\frac{1}{\rho_0}\frac{\partial p}{\partial y}}^{V_{prsgrd}} + \overbrace{\frac{\partial}{\partial x}\left(A_h\frac{\partial v}{\partial x}\right) + \frac{\partial}{\partial y}\left(A_h\frac{\partial v}{\partial y}\right)}^{V_{hvisc}} + \overbrace{\frac{\partial}{\partial z}\left(A_z\frac{\partial v}{\partial z}\right)}^{V_{vvisc}} \tag{8}$$

In Eq. (7) and Eq. (8), $u$, $v$, and $w$ are the cross-strait (positive/offshore), along-strait (positive/northward), and vertical (positive/upward) velocity components, and $x$, $y$, and $z$ are the corresponding coordinates (Fig. 1b). $t$ is time, $p$ is pressure, $f$ is the Coriolis parameter, and $\rho_0$ is a constant reference density which equals 1025 kg m$^{-3}$. $A_h$ and $A_z$ are the horizontal and vertical turbulent viscosity coefficients, respectively. The acceleration term (accel) is on the left-hand side, and the right-hand side presents the total advection term (adv), Coriolis term (cor), pressure gradient term (prsgrd), horizontal viscosity term (hvisc), and vertical viscosity term (vvisc), within the momentum budget as denoted in the equations, with the capital $U$ and $V$ indicating the corresponding terms in the cross-strait and along-strait directions, respectively.

The wind stress induced vertical viscosity term changed sign at March 30 for both the cross-strait and along-strait budget in the surface layer (Fig. 8a and b), when the northeasterly wind relaxed to nearly zero. As a result, the cross-strait momentum balance turned to be dominated almost by the geostrophic balance at that day, indicating the significant role of the geostrophic adjustment. With the increasing southwesterly wind from March 31 to April 2, the cross-strait surface budget became a balance among the pressure gradient term, Coriolis term, and the vertical viscosity term, while the along-strait surface budget was nearly dominated by the Coriolis term and vertical viscosity term. Consequently, in the surface layer, the geostrophic adjustment occurred dominantly at March 30 when the wind in the TWS was nearly
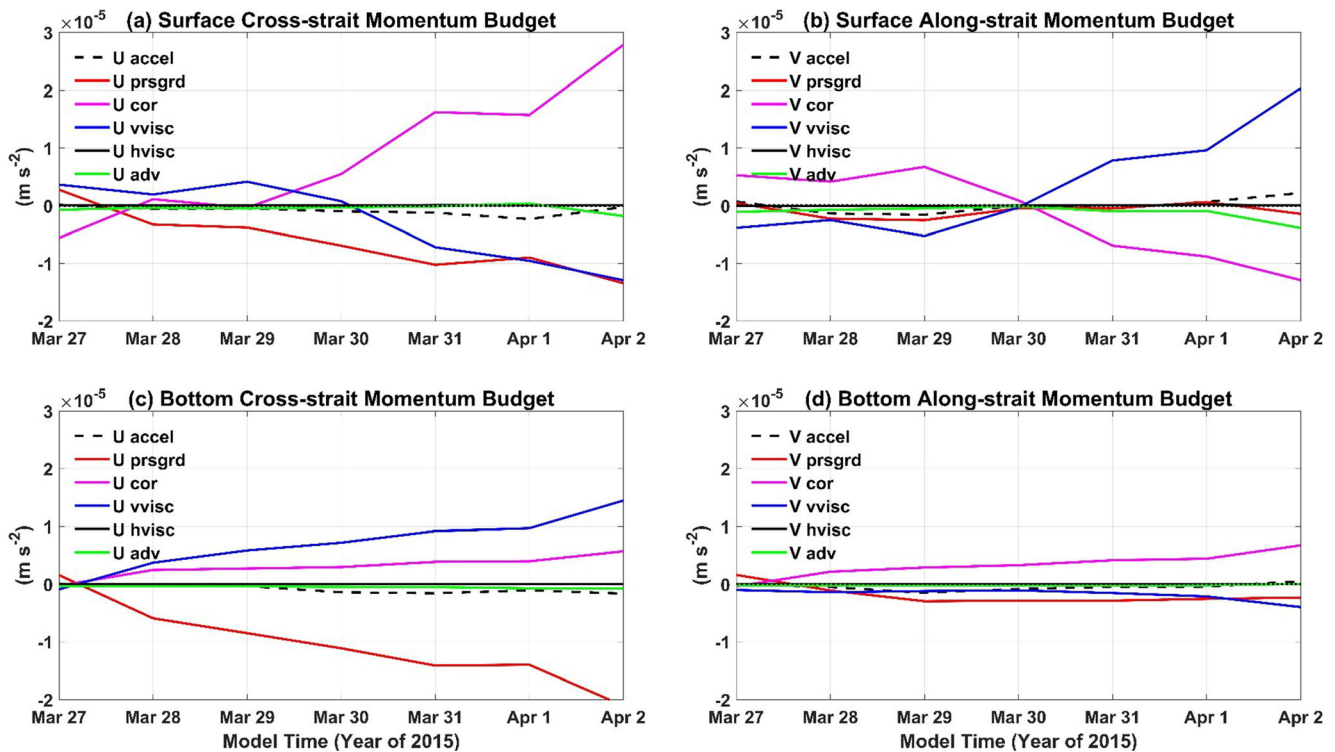
**Fig. 8** Modeled time series of the cross-strait (**u**) momentum budget terms ((**a**) for the surface layer and c for the bottom layer, offshore is positive and onshore is negative; units: m s$^{-2}$) and along-strait (v) momentum budget terms ((**b**) for the surface layer and d for the bottom layer, northward is positive and southward is negative; units: m s$^{-2}$) at station Y12a during March 27 to April 2, 2015. Accel, prsgrd, cor, vvisc,

hvisc, and adv denote the acceleration term, pressure gradient term, Coriolis term, vertical viscosity term, horizontal viscosity term, total advection term in Eq. (7) and Eq. (8). The u, v direction and location of station Y12a are shown in Fig. 1. Model results with weak nudging of 120-day relaxation time starting at March 1, 2015 are used for the analysis

zero, then the surface Ekman effects from the increasing southwesterly wind was becoming more and more significant comparing with the geostrophic adjustment during March 31 to April 2, until the development of the cold water anomalies in the middle layer.

In the bottom layer, the momentum budget was always a balance between the pressure gradient term, Coriolis term, and the vertical viscosity term from March 27 to April 2, despite of the wind transition process (Fig. 8c and d). The increasing positive cross-strait bottom vertical viscosity term (blue line in Fig. 8c) corresponded to the enhancing onshore velocity component in the lower layers (Fig. 7a–d) from the supplementary bottom onshore Ekman transport of the southwesterly wind.

## 4.2 Thermal diagnosis

The physical effects on the variation of temperature distribution can be demonstrated clearly from the model result diagnostic (Eq. (9)). The diagnosis also uses model results with weak SST nudging (120-day relaxation time starting at March 1, 2015) to decrease the artificial effects on the physical process as Section 4.1. The left-hand side of Eq. (9) is the

tendency term. The right-hand side includes the advection and diffusion terms.

$$\frac{\partial T}{\partial t} = -\left(u\frac{\partial T}{\partial x} + v\frac{\partial T}{\partial y} + w\frac{\partial T}{\partial z}\right) + Dif_h + Dif_v \quad (9)$$

where $T$ is temperature and $u$, $v$, $w$, and $t$ are as aforementioned descriptions for Eq. (7) and Eq. (8). $(-u\partial T/\partial x - v\partial T/\partial y)$ and $(-w\partial T/\partial z)$ are the horizontal and vertical advection terms, respectively. $(-u\partial T/\partial x)$ and $(-v\partial T/\partial y)$ are the cross-strait (**u**) and along-strait (**v**) components of the horizontal advection term, respectively. $Dif_h$ and $Dif_v$ are the horizontal and vertical diffusion terms, respectively, whereas the latter includes the net heat flux at the surface.

The distributions of the advection terms in Eq. (9) along section Y1 on April 1 are shown in Fig. 9. On March 31, the wind in the TWS switched from northeasterly to southwesterly (Fig. 3a). The cross-strait component of the horizontal advection term had a significant warming effect in the lower layer (roughly > 15-m depth) and a relatively weak cooling effect on the upper 15-m layer on April 1 (Fig. 9a). This was consistent with the corresponding offshore current pattern described in Section 4.1. The along-strait horizontal advection imposed a cooling effect on the inner stations Y11 and Y12a
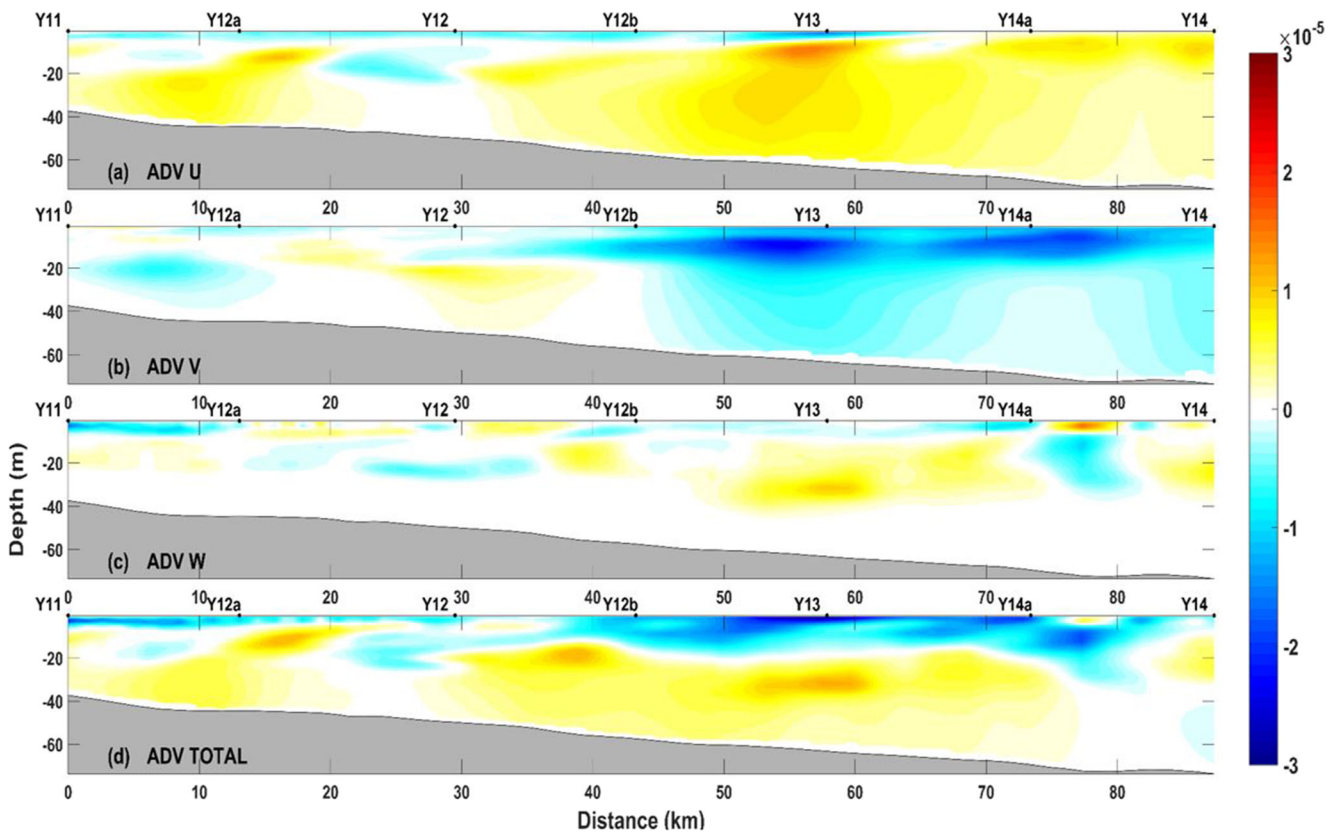
**Fig. 9** Vertical distributions of the cross-strait (**a**) and along-strait (**b**) components of the horizontal advection term, vertical advection term (**c**) as well as the total advection term (**d**) in Eq. (9) along section Y1 on April 1 (units: °C/s). The location of section Y1 is shown in Fig. 1c. Model results with weak nudging of 120-day relaxation time starting at March 1, 2015 are used for the analysis

(Fig. 9b), which might be due to the southward current there (Fig. 7e). Compared with the horizontal term, the vertical advection term exhibited a relatively weak thermal effect on the section (Fig. 9c). It is worth noting that there were parallel patchiness regions about 10 m thick and 10 km wide with different signs, which may be related to small-scale physical processes, which require further study. The thermal effects of the total advection had a warming effect on the bottom 20-m layer between stations Y11 and Y13, as well as a relatively weak cooling effect on the upper 15-m layer (Fig. 9d).

The distribution of vertical diffusion along section Y1 on April 1 is shown in Fig. 10. The vertical diffusion exhibited a significant warming effect on the top 10 m of the surface layer, which was likely induced by the downward net heat flux during this period (Fig. 10), whereas the horizontal diffusion had a minimal contribution to the variation in temperature (not shown here). Figure 10 shows that the significantly increased heat within the surface layer cannot be transferred easily down to the deeper layers, suggesting the damped vertical mixing process during the middle-layer cold water anomalies phenomenon.
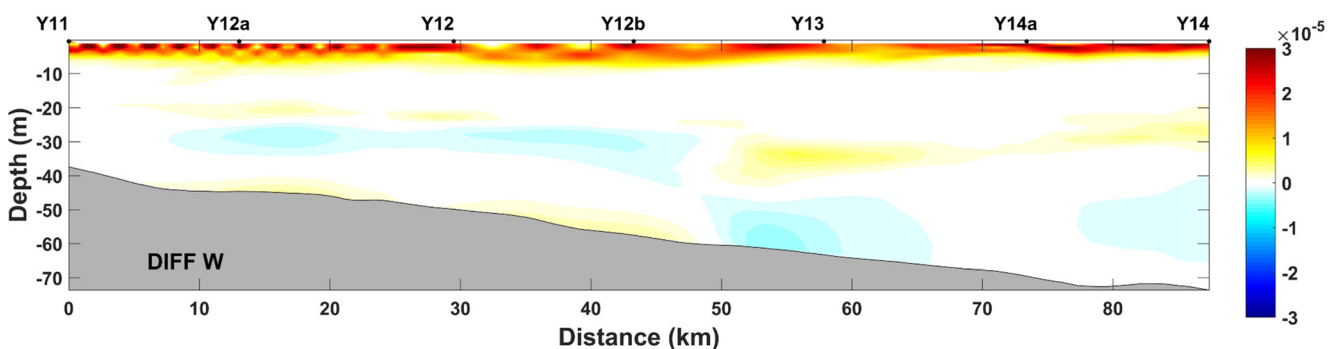


**Fig. 10** Vertical distribution of the vertical diffusion term in Eq. (9) along section Y1 on 1 April (units: °C/s). The location of section Y1 is shown in Fig. 1c. Model results with weak nudging of 120-day relaxation time starting at March 1, 2015 are used for the analysis

The diagnostic analysis showed that the cross-strait horizontal advection and vertical diffusion/net heat flux imposed positive thermal contributions to the 20-m-thick bottom layer and the 10-m-thick upper layer of section Y1, respectively, prior to April 2, whereas in the middle layer, the warming effect was not so significant, resulting in the presence of the middle-layer cold water anomaly.

## 5 Conclusions

In situ observations found uncharacteristic cold water anomalies in the middle layer in the northern TWS in the spring of 2015. To the best of our knowledge, prior to this study, the scenarios and related mechanisms have not been reported unambiguously. This study employed a three-dimensional operational numerical model, in which the sea-surface net heat flux was justified by nudging the appropriate MUR SST, to reproduce and study the phenomena. Both modeled dynamic process analysis and thermal diagnosis were used to explain the intrinsic mechanisms behind the cold water anomalies in the middle layer. The results illustrated that when the monsoon in the TWS switched from northeasterly to southwesterly, an offshore velocity component in the upper layer was induced by the geostrophic adjustment at first and then by the Ekman transport. Meanwhile, the onshore movement of the warm water from eastern bottom strait was led by the supplementary bottom onshore Ekman transport. At the same time, the increasing net heat flux led to significant temperature increases in the surface layer, whereas in the middle layer, the warming effect was not particularly significant, causing the cold water anomaly in the middle layer.

However, middle-layer cold water anomalies with different magnitudes were found in the observational sections in the spring of 2015 (Fig. 4j–r). The reasons for the most significant cold water anomaly occurring in section Y1 require further research. The magnitude and location of the offshore branch of the CCC that caused the offshore extension of cold water possibly affected those of the middle-layer cold water anomalies in the TWS, which also requires further study.

## References

Barnier B, Siefridt L, Marchesiello P (1995) Thermal forcing for a global ocean circulation model using a three-year climatology of ECMWF analyses. J Mar Syst 6:363–380. https://doi.org/10.1016/0924-7963(94)00034-9

Chapman DC (1985) Numerical treatment of cross-shelf open boundaries in a barotropic coastal ocean model. J Phys Oceanogr 15:1060–1075. https://doi.org/10.1175/1520-0485(1985)015<1060:Ntocso>2.0.Co;2

Chen XY, Qiao FL, Ge RF, Xia CS, Yuan YL (2006) Development of subsurface warm water in the East China Sea in fall. J Geophys Res-Oceans 111:15. https://doi.org/10.1029/2005jc003163

Chen ZY, Yan XH, Jiang YW (2014) Coastal cape and canyon effects on wind-driven upwelling in northern Taiwan Strait. J Geophys Res-Oceans 119:4605–4625. https://doi.org/10.1002/2014jc009831

Cushman-Roisin B, Beckers J-M (2011) Chapter 15 - dynamics of stratified rotating flows. In: Cushman-Roisin B, Beckers J-M (eds) International Geophysics, vol 101. Academic Press, pp 473–520. https://doi.org/10.1016/B978-0-12-088759-0.00015-8

Ding ZX, Lan SF (1995) A preliminary analysis of the distribution of the inverse types of temperature and its formative causes in the southern yellow sea and the east china seas in spring and winter. Mar Sci 19:35–39 (in Chinese with English abstract)

Egbert GD, Erofeeva SY (2002) Efficient inverse modeling of barotropic ocean tides. J Atmos Ocean Technol 19:183–204. https://doi.org/10.1175/1520-0426(2002)019<0183:Eimobo>2.0.Co;2

Fairall CW, Bradley EF, Rogers DP, Edson JB, Young GS (1996) Bulk parameterization of air-sea fluxes for Tropical Ocean Global Atmosphere Coupled Ocean Atmosphere Response Experiment. J Geophys Res-Oceans 101:3747–3764. https://doi.org/10.1029/95jc03205

Flather RA (1976) A tidal model of northwest European continental shelf memo. Soc Roy Sci Liege 6:141–164

Guan BX (1999) Phenomenon of the inversion thermocline in winter in the coastal water of the west of east china sea and its relation to circulation. J Oceanogr Huanghai Bohai Seas 17:1–7 (in Chinese with English abstract)

Hao JJ, Chen YL, Wang F (2010) Temperature inversion in China seas. J Geophys Res-Oceans 115:12. https://doi.org/10.1029/2010jc006297

Hong HS, Chai F, Zhang CY, Huang BQ, Jiang YW, Hu JY (2011) An overview of physical and biogeochemical processes and ecosystem dynamics in the Taiwan Strait. Cont Shelf Res 31:S3–S12. https://doi.org/10.1016/j.csr.2011.02.002

Hu JY, Kawamura H, Hong HS, Pan WR (2003) A review of research on the upwelling in the Taiwan Strait. Bull Mar Sci 73:605–628

Hu JY, Kawamura H, Li CY, Hong HS, Jiang YW (2010) Review on current and seawater volume transport through the Taiwan Strait. J Oceanogr 66:591–610. https://doi.org/10.1007/s10872-010-0049-1

Hu JY et al (2011) Variable temperature, salinity and water mass structures in the southwestern Taiwan Strait in summer. Cont Shelf Res 31:S13–S23. https://doi.org/10.1016/j.csr.2011.02.003

Jan S, Wang J, Chern CS, Chao SY (2002) Seasonal variation of the circulation in the Taiwan Strait. J Mar Syst 35:249–268. https://doi.org/10.1016/s0924-7963(02)00130-6

Jan S, Sheu DD, Kuo HM (2006) Water mass and throughflow transport variability in the Taiwan Strait. J Geophys Res-Oceans 111:15. https://doi.org/10.1029/2006jc003656

Jiang YW, Chai F, Wan ZW, Zhang X, Hong HS (2011) Characteristics and mechanisms of the upwelling in the southern Taiwan Strait: a three-dimensional numerical model study. J Oceanogr 67:699–708. https://doi.org/10.1007/s10872-011-0080-x

Liao EH, Jiang YW, Li L, Hong HS, Yan XH (2013) The cause of the 2008 cold disaster in the Taiwan Strait. Ocean Model 62:1–10. https://doi.org/10.1016/j.ocemod.2012.11.004

Lin XY, Yan XH, Jiang YW, Zhang ZC (2016) Performance assessment for an operational ocean model of the Taiwan Strait. Ocean Model 102:27–44. https://doi.org/10.1016/j.ocemod.2016.04.006

Lu WF, Yan XH, Jiang YW (2015) Winter bloom and associated upwelling northwest of the Luzon Island: a coupled physical-biological

modeling approach. J Geophys Res-Oceans 120:533–546. https://doi.org/10.1002/2014jc010218

Oey L, Chang YL, Lin YC, Chang MC, Xu FH, Lu HF (2013) ATOP - the advanced Taiwan Ocean prediction system based on the mpiPOM. Part 1: model descriptions, analyses and results. Terr Atmos Ocean Sci 24:137–158. https://doi.org/10.3319/TAO.2012.09.12.01(Oc)

Oey LY, Chang YL, Lin YC, Chang MC, Varlamov S, Miyazawa Y (2014) Cross flows in the Taiwan Strait in winter*. J Phys Oceanogr 44:801–817. https://doi.org/10.1175/jpo-d-13-0128.1

Qiu Y, Xu JD, Guo XG, Lin N, Zhou XW (2012) Temperature inversion in the Taiwan Strait during northeast monsoon. Acta Oceanol Sin 34:13–22 (in Chinese with English abstract)

Shchepetkin AF, McWilliams JC (2003) A method for computing horizontal pressure-gradient force in an oceanic model with a non-aligned vertical coordinate. J Geophys Res Oceans 108:34. https://doi.org/10.1029/2001jc001047

Shchepetkin AF, McWilliams JC (2005) The regional oceanic modeling system (ROMS): a split-explicit, free-surface, topography-following-coordinate oceanic model. Ocean Model 9:347–404. https://doi.org/10.1016/j.ocemod.2004.08.002

Song Y, Haidvogel D (1994) A semi-implicit ocean circulation model using a generalized topography-following coordinate system. J Comput Phys 115:228–244. https://doi.org/10.1006/jcph.1994.1189

Thadathil P, Gosh AK (1992) Surface layer temperature inversion in the Arabian Sea during winter. J Oceanogr 48:293–304

Ueno H, Yasuda I (2005) Temperature inversions in the subarctic North Pacific. J Phys Oceanogr 35:2444–2456. https://doi.org/10.1175/jpo2829.1

Wang ZS, Xu BC, Zou EM, Liao QY (2002) Formation causes of the intermediate cold water in the Northwestern East China Sea. Adv Mar Sci 20:68–72 (in Chinese with English abstract)

Wang J, Hong HS, Jiang YW, Chai F, Yan XH (2013) Summer nitrogenous nutrient transport and its fate in the Taiwan Strait: a coupled physical-biological modeling approach. J Geophys Res-Oceans 118:4184–4200. https://doi.org/10.1002/jgrc.20300

Wang J, Hong HS, Jiang YW (2016) A coupled physical-biological modeling study of the offshore phytoplankton bloom in the Taiwan Strait in winter. J Sea Res 107:12–24. https://doi.org/10.1016/j.seares.2015.11.004

Willmott CJ (1981) On the validation of models physical geography. 2:184–194. https://doi.org/10.1080/02723646.1981.10642213

Wu CR, Chao SY, Hsu C (2007) Transient, seasonal and interannual variability of the Taiwan Strait current. J Oceanogr 63:821–833. https://doi.org/10.1007/s10872-007-0070-1

Xiao H, Guo XG, Wu RS (2002) Summarization of studies on hydrographic characteristics in Taiwan Strait. J Oceanogr Taiwan Strait 21:126–138 (in Chinese with English abstract)

Xu BC, Wang ZS, Zou EM, Liao QY (2000) The spatial and temporal variations of the characteristics of the intermediate cold water in the northwest of the East China Sea. J Oceanogr Huanghai Bohai Seas 18:1–7 (in Chinese with English abstract)

Yan WB (1991) The inversion thermocline in Taiwan Strait. J Oceanogr Taiwan Strait 10:334–337 (in Chinese with English abstract)

Yang JY (2007) An oceanic current against the wind: how does Taiwan island steer warm water into the East China Sea? J Phys Oceanogr 37:2563–2569. https://doi.org/10.1175/jpo3134.1